Multidimensional compressed sensing to advance 23 Na multi-quantum coherences MRI

Christian Licht, Simon Reichert, Maxime Guye, Lothar Schad, Stanislas Rapacchi

Received: 13 May 2023 | Revised: 13 September 2023 | Accepted: 9 October 2023

DOI: 10.1002/mrm.29902

RESEARCH ARTICLE

Magnetic Resonance in Medicine

Multidimensional compressed sensing to advance ^{23}Na multi-quantum coherences MRI

Christian Licht[1,2] | **Simon Reichert**[1,2] | **Maxime Guye**[3,4] | **Lothar R. Schad**[1,2] | **Stanislas Rapacchi**[3,4]

[1]Computer Assisted Clinical Medicine, Medical Faculty Mannheim, Heidelberg University, Mannheim, Germany

[2]Mannheim Institute for Intelligent System in Medicine, Medical Faculty Mannheim, Mannheim, Germany

[3]Aix-Marseille Univ, CNRS, CRMBM, Marseille, France

[4]APHM, Hôpital Universitaire Timone, CEMEREM, Marseille, France

Correspondence
Christian Licht, Computer Assisted Clinical Medicine, Medical Faculty Mannheim, Heidelberg University, Theodor-Kutzer-Ufer 1-3, 68167 Mannheim, Germany.
Email: Christian.Licht@medma.uni-heidelberg.de

Funding information
ISMRM Research Exchange 2022; PROCOPE Mobility 2022; French government under the "Programme d'Investissement d'Avenir", Excellence Initiative of Aix-Marseille University-A*MIDEX (AMX-19IET-004), 7 TEAMS Chair

Abstract

Purpose: Sodium (^{23}Na) multi-quantum coherences (MQC) MRI was accelerated using three-dimensional (3D) and a dedicated five-dimensional (5D) compressed sensing (CS) framework for simultaneous Cartesian single (SQ) and triple quantum (TQ) sodium imaging of in vivo human brain at 3.0 and 7.0 T.

Theory and Methods: 3D ^{23}Na MQC MRI requires multi-echo paired with phase-cycling and exhibits thus a multidimensional space. A joint reconstruction framework to exploit the sparsity in all imaging dimensions by extending the conventional 3D CS framework to 5D was developed. 3D MQC images of simulated brain, phantom and healthy brain volunteers obtained from 3.0 T and 7.0 T were retrospectively and prospectively undersampled. Performance of the CS models were analyzed by means of structural similarity index (SSIM), root mean squared error (RMSE), signal-to-noise ratio (SNR) and signal quantification of tissue sodium concentration and TQ/SQ ratio.

Results: It was shown that an acceleration of three-fold, leading to less than 2×10 min of scan time with a resolution of $8 \times 8 \times 20\,\text{mm}^3$ at 3.0 T, are possible. 5D CS improved SSIM by 3%, 5%, 1% and reduced RMSE by 50%, 30%, 8% for in vivo SQ, TQ, and TQ/SQ ratio maps, respectively. Furthermore, for the first time prospective undersampling enabled unprecedented high resolution from $8 \times 8 \times 20\,\text{mm}^3$ to $6 \times 6 \times 10\,\text{mm}^3$ MQC images of in vivo human brain at 7.0 T without extending acquisition time.

Conclusion: 5D CS proved to allow up to three-fold acceleration retrospectively on 3.0 T data. 2-fold acceleration was demonstrated prospectively at 7.0 T to reach higher spatial resolution of ^{23}Na MQC MRI.

KEYWORDS

compressed sensing, MRI, neuroimaging, single and triple quantum imaging, sodium multi-quantum coherences

Lothar R. Schad and Stanislas Rapacchi contributed equally to this work.

1 | INTRODUCTION

Sodium (^{23}Na) MRI is a promising tool to probe tissue ionic homeostasis, which in return could provide valuable information on tissue viability.[1-3] Sodium MRI is attractive for its unique specificity to directly characterize tissues ionic homeostasis from the linear correlation between MR signal and the sodium concentration in vivo. Indeed, with proper calibration and ultra-short echo times, ^{23}Na MRI can map apparent quantitative tissue sodium concentration (TSC).[4-7] The cell's vitality is closely related to the sodium concentration and thus, offers great potentials to be a clinical marker for disease states.[8] Sodium MRI has been used to assess various types of cancer,[9] brain tumors,[10,11] in neurodegenerative diseases such as Alzheimer's disease,[12] or multiple sclerosis.[13,14] Thanks to the advent of ultra-high field (≥7.0 T) MRI and associated coil designs for dual-tuned ^{1}H/^{23}Na complementary imaging, ^{23}Na has received increased interest in recent years.[8]

Besides TSC quantification, ^{23}Na MRI also offers MR contrasts that could further inform on tissue's health and evolution. In particular, ^{23}Na nuclei exhibit a quadrupolar moment leading to multi-quantum coherences (MQC). Under certain conditions, one can observe besides the single quantum (SQ), also double- (DQ), and triple quantum (TQ) coherences. TQ coherences arise from the biexponential relaxation observable in slow motion regimes such as white matter (WM), gray matter (GM) and is sensitive to the nucleus' molecular environment.[15] Beyond sodium concentration, the TQ signal of ^{23}Na holds promises for novel or even complementary information to conventional ^{23}Na MRI. It has been shown that the TQ signal is sensitive to changes in the sodium surroundings much earlier than conventional ^{23}Na MRI[16] and scales linearly with the intracellular sodium concentration, as it has been shown by Schepkin et al.[17] in rat hearts. Conclusively, studying the full ^{23}Na MR signal by leveraging MQC imaging techniques[18] to jointly acquire SQ and TQ signal components could provide more and/or novel information about the tissue, the macroscopic sodium environment and the cell's vitality overall.

^{23}Na MQC imaging is challenging as it suffers from lower NMR sensitivity and requires radio frequency (RF) phase-cycling, severely prolonging acquisition time and therefore limiting spatial resolution. Additionally, ^{23}Na MQC MRI requires strong 90° RF pulses which are limited due to SAR restrictions. So far the feasibility of ^{23}Na TQ imaging has been demonstrated in the brain,[18-21] the knee[22] and in spinal disc tissue.[23] Additionally, Boada et al.[24] demonstrated TQ imaging of primary brain tumors and proposed that it is a valuable tool to monitor the changes of intracellular sodium content that relates to neoplastic changes.

Compressed sensing (CS) has been established to speed up MR imaging by undersampling the acquisition. The pseudo-randomly undersampled data are iteratively reconstructed to provide images that fulfill sparsity in one or multiple transformed domains from the image.[25] CS has demonstrated to improve conventional sodium imaging of the knee,[26] of multichannel breast data[27] and of the brain,[28-30] also including CNN postprocessing.[31] To our knowledge, however, CS has not been applied to ^{23}Na MQC MRI yet. As such, this technique is a suitable candidate to accelerate ^{23}Na MQC imaging, too. Three-dimensional (3D) MQC imaging acquires 3D volumetric images along the echo time for a minimum of 12 RF phase-cycling steps, yielding a five-dimensional (5D) signal structure. This signal is a superposition of different signal components consisting of the SQ, DQ, and TQ signals. Hence, ^{23}Na MQC MRI spans a redundant multidimensional space which can be jointly reconstructed by exploiting sparsity in each imaging dimension and thus, fulfills basic CS requirements.[32]

It has been shown that optimal reconstruction results are achieved by exploiting sparsity in all imaging dimensions.[33] Spatial sparsity can be efficiently exploited by minimizing the energy of the gradients, total variation (TV).[34] Based on the high similarity of the successive multi-echo images, the temporal information is redundant.[35] Hence, the temporal signal evolution can be represented with only a few coefficients. Additionally, ^{23}Na MQC MRI requires RF phase-cycling. According to the Fleysher phase-cycling scheme,[36] applying a one-dimensional Fourier transform along the equidistant phase-cycle dimension reveals the individual MQC spectra. Hence, the spectra information can contain intrinsically sparser information than the superimposed ^{23}Na MQC MR signal. Following, the temporal and spectral information can be additionally leveraged to enhance reconstruction performance of undersampled ^{23}Na MQC k-space data.

Conclusively, for the first time we present reconstruction of highly multidimensional ^{23}Na MQC MRI by leveraging conventional 3D and joint 5D multidimensional CS in retrospectively undersampled numerical simulations, phantom and in-vivo brain data acquired at 3.0 T and prospectively undersampled in vivo brain data acquired at 7.0 T.

2 | METHODS

2.1 | Image acquisition

2.1.1 | Numerical simulation

^{23}Na MQC brain data were simulated based on a numerical phantom of the three-compartment

TABLE 1 Sequence parameters for numerical simulations, phantom study at 3.0 T, retrospective in vivo study at 3.0 T and prospective in vivo study at 7.0 T.

Parameter	Numerical simulation 3.0 T	Phantom 3.0 T	In vivo 3.0 T	In vivo 7.0 T
Field of view (mm^3)	181×217×181	190×190×200	230×230×160	220×220×220
Matrix size	30×30×20	24×24×10	24×24×8	36×36×22
TE_1/ ΔTE (ms)	1.0/ 5.0	1.67/ 6.4	1.62/ 6.2	1.16/ 4.5
Bandwidth (Hz/px)	—	200	220	330
TR (ms)	200	150	150	196
Pulse duration (ms)	0[a]	0.5	0.5	0.7
Evolution time (ms)	10	12.1	10.1±2.12	10
Averages	1	17	11	7
TA (min)	—	2×60	2×31	2×34

Abbreviations: FoV, field of view; TE, echo time; TR, pulse repetition time.
[a] Hard pulse approximation was used.

segmentation from Collins et al.[37] utilizing the Fleysher phase-cycle scheme.[36] Phantom brain data were resized via interpolation of nearest neighbour to approximate ^{23}Na MQC images with a resolution of $7 \times 7 \times 10\ mm^3$. The synthetic brain was divided into a three-compartment model consisting of WM, GM and cerebrospinal fluid (CSF). T_1 and T_2^* values for each compartment were assigned as:[4,38] (T_1/ T_{2f}^*/ T_{2s}^* in ms) for WM (34/ 3.4/ 18), GM (32/ 3.6/ 15), and CSF (55/ 51/ 51) with a magnetic field strength of $B_0 = 3.0$ T. ^{23}Na NMR dynamics were simulated using the irreducible spherical tensor operator formalism of Hancu et al.[39] and the evolution equations of van der Maarel,[40] hard pulse approximation. Random Gaussian noise with varying power defined as $P = \text{mean}(\eta^2)$ was added. CRISTINA simulation and acquisition parameters were summarized in Table 1.

2.1.2 | Phantom and in vivo

Imaging was performed on an NaCl/agarose phantom and six healthy volunteers at 3.0 T (four volunteers) and 7.0 T (three volunteers) MRI (Siemens MAGNETOM Trio and Magnetom) systems, each equipped with a 1Tx/Rx dual-tuned ^{1}H/^{23}Na head coil (3.0 T: RAPID Biomedical, 7.0 T: QED). The study was approved by local ethical committee and volunteers were recruited after providing written informed consent according to the Declaration of Helsinki. A custom 3D multi-echo multi-quantum sequence termed CRISTINA,[18] was used to obtain the single- and triple-quantum filtered images with an optimized 2×6-steps phase cycle.[41] Prior to each measurement, B_0 shimming was performed to minimize field inhomogeneities. RF pulses' flip angle was globally calibrated. CRISTINA evolution time for 3.0 T acquisitions was determined via a global TQ time proportional phase incrementation[42] spectroscopic prescan and a subsequent offline fit was used to map the TQ signal evolution over time. The evolution time for 7.0 T scans was preset to 10 ms.[41] In order to validate accurate signal intensity reconstruction, fully sampled ($R = 1$) images of a phantom consisting of nine tubes (350-mL each) with varying agarose (0%, 2%, and 4%) and sodium (50, 100, 150 mM) concentrations were obtained. For 3.0 T in vivo acquisitions, a two-dimensional anatomical ^{1}H T_1 scan was performed with a nominal resolution of $1 \times 1 \times 5\ mm^3$ within 4 min. For 7.0 T acquisitions, a prototype CS 3D anatomical ^{1}H MP2RAGE[43] scan was performed with a nominal resolution of $1 \times 1 \times 1\ mm^3$ within 4 min. Four vials were placed next to the head, with concentrations of agarose and ^{23}Na of: (4%; 100 mM), (4%; 50 mM), (2%; 100 mM), and (2%; 50mM).

Numerical simulations, phantom and 3.0 T in vivo data were retrospectively undersampled by factors of R = 2–7 and in vivo 7.0 T data were prospectively undersampled by $R = 2$ and one dataset $R = 3$ (matrix size $30 \times 30 \times 26$). 3D variable-density random sampling patterns (undersampling solely performed along ky and kz) following a Poisson distribution[44] were used to retrospectively and prospectively undersample ^{23}Na MQC k-space data. Undersampling patterns were alternated along phase-cycling to enhance incoherence. The level of incoherence was measured by computing the number of points that were sampled at least once during the phase-cycling, divided by the size of the k-space matrix.

2.2 | Image reconstruction

The proposed workflow for the project is depicted in Figure 1. Multiple repetitions obtained with the same undersampling pattern were averaged before reconstruction. Each phase-cycle dataset, χ_0 and χ_{90}, were reconstructed individually. To solve the optimization problems stated in Equation (1), the Split Bregman method was extended based on the algorithm proposed by Goldstein et al.,[45] either to solve for 3D or 5D signal inputs. Subsequently, the constrained optimization algorithm for 3D and 5D CS aims to solve the following problems:

$$\begin{aligned}
&\textbf{3D CS}: \quad \min_u \ \lambda_p||(\nabla_x u, \nabla_y u, \nabla_z u)||_2 \\
&\qquad s.t. \ \ ||\Phi_F(u) - f||_2^2 < \sigma^2, \\
&\textbf{5D CS}: \quad \min_u \ \lambda_p||(\nabla_x u, \nabla_y u, \nabla_z u)||_2 + \lambda_{TE}||\Psi_{TE} u||_2 + \lambda_\varphi||\Psi_\varphi u||_2 \\
&\qquad s.t. \ \ ||\Phi_F(u) - f||_2^2 < \sigma^2,
\end{aligned} \tag{1}$$

with u being the target image to reconstruct, ∇ represents the first-order derivative along the spatial dimensions, x, y and z, Ψ the Fourier transform along the temporal and phase cycle dimension and λ being the sparsity weighting parameter for spatial, $p = [x, y, z]$, multi-echo, TE, and phase-cycle dimension, ϕ. The optimal values for each regularization term were explicitly computed by leveraging shrinkage operations[45] that used different sparsity thresholds (β). The second term corresponds to the data fidelity with Φ_F indicating the partial Fourier transform followed by random undersampling, f representing the measured data in frequency domain and σ^2 being the variance of the signal noise. 3D CS reconstructed each 3D volume separately.

Reconstruction performances of Wavelet transform and TV were tested, with both performing similar (Figure S1). Hence, TV was utilized as the transform to exploit sparsity in the spatial domains. The latter regularization terms in the 5D CS optimization problem exploit sparsity along the multi-echo and phase-cycle dimension. By computing the one-dimensional Fourier transform along the multi-echo and phase-cycle dimensions separately, a sparser domain is obtained (Figure S2). Based on empirical evaluation, spatial sparsity term weighting was set to $\lambda_p = 1$, with the optimal threshold being $\beta_p = 1.5$ and $\beta_p = 0.3$ for 3D and 5D CS, respectively. However, multidimensional sparsity is challenging to balance and therefore, additional sparsity term weightings for 5D CS were determined by performing 144 CS reconstructions with weighting factors $\lambda_{TE} = 0.1 \ldots 1.2$ and $\lambda_\phi = 1 \ldots 2.1$ (12×12 combinations), enabling to find the optimal regularization parameters (Figure S3). Identically, optimal sparsity thresholds for the additional terms in the 5D CS model were empirically determined with $\beta_{\mathrm{TE}} = 0.1 \ \ldots \ 1.2$ and $\beta_\phi = 1.0 \ \ldots \ 2.1$ (Figure S4). Based on the empirical results, optimal sparsity weightings were $\lambda_{\mathrm{TE}} = 0.2$ and $\lambda_\phi = 1.9$ and optimal sparsity thresholds were $\beta_{\mathrm{TE}} = 0.5$ and $\beta_\phi = 1.6$. Reconstruction times for numerical simulations were 550 s for 3D (50 iterations) and 227 s for 5D CS (300 iterations), and for 3.0 T in vivo 313 s for 3D (100 iterations) and 55 s (250 iterations) for 5D CS.

2.3 | Image processing

k-Space was zero-padded with the addition of 3D Hamming windowing. The first two echoes of CRISTINA phase data were used to compute a 3D B0 map to obtain the signal off-resonances for combination of the two phase cycles (χ_0 and χ_{90}) according to the method of Fleysher et al.[36] Finally, applying a Fourier transform along the phase-cycle dimension revealed the SQ and TQ spectra. Reconstructed SQ and TQ images were fitted to the MQC bi-exponential model given in Equation (2).

$$\begin{aligned}
&\textbf{TQ}: \quad A_{\mathrm{TQ}}\left(e^{-\frac{\mathrm{TE}}{T_{2s}^*}} - e^{-\frac{\mathrm{TE}}{T_{2f}^*}}\right)e^{-\frac{\tau_1}{T_{2s}^*}} + \mathrm{DC}_{\mathrm{TQ}} \\
&\textbf{SQ}: \quad \left(A_{\mathrm{SQ}_1}e^{-\frac{\mathrm{TE}+\tau_1+\tau_2}{T_{2s}^*}} + A_{\mathrm{SQ}_2}e^{-\frac{\mathrm{TE}+\tau_1+\tau_2}{T_{2f}^*}}\right)e^{-\frac{\mathrm{TE}+\tau_1+\tau_2}{T_{2s*}}} + \mathrm{DC}_{\mathrm{SQ}}
\end{aligned} \tag{2}$$

with A_{TQ}, A_{SQ_1}, A_{SQ_2} being triple- and single-quantum amplitude terms (slow and fast), $\mathrm{DC}_{\mathrm{TQ,SQ}}$ = DC offset accounting for noise, $T_{2s}^* = T_2^*$ slow, $T_{2f}^* = T_2^*$ fast, τ_1 = evolution time and τ_2 = mixing time (time between second and third RF pulse). The value of TQC at TE = 0 ms is 0 from theory and was added to the multi-echo data to enhance the fit. First, the voxel-wise multiparametric fit of TQ was performed followed by the SQ fit with updated initial values, using nonlinear least squares solver in Matlab (R2020a, Mathworks) leveraging parallel computing, providing T_{2s}^* and T_{2f}^* maps.

2.4 | Image analysis

Quantitative analysis of the phantom study was performed in a predetermined region of interest (ROI) that was drawn over each tube on a single central slice, avoiding edges. ROI mean values served to compute SQ and TQ/SQ ratios for each tube. Linear regression between SQ and prior known sodium concentration, as well as TQ/SQ ratio and

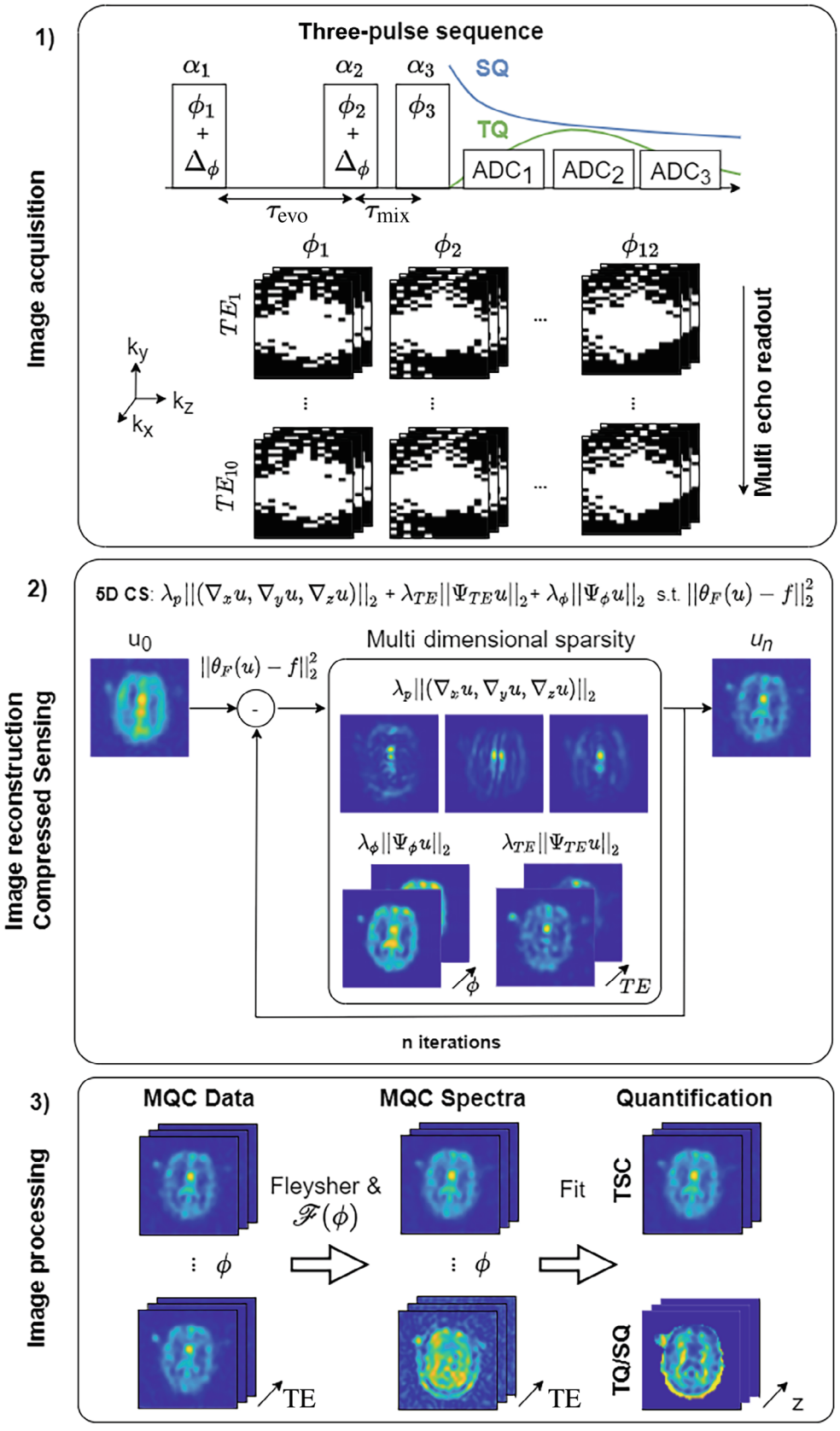

FIGURE 1 Workflow including variable density undersampling and compressed sensing (CS) reconstruction for accelerated ^{23}Na multi-quantum coherences (MQC) MRI. (1) Image acquisition is performed by utilizing a three-pulse radiofrequency phase-cycled three-dimensional (3D) Cartesian multi-echo readout sequence, yielding a five-dimensional (5D) signal structure involving 3D spatial, multi-echo and phase-cycle dimension. Undersampling is performed along ky and kz (phase-encoding) by alternating the patterns along the phase-cycle dimension, ϕ. (2) Undersampled high-multidimensional k-space data is reconstructed leveraging a conventional 3D or a custom build 5D CS algorithm that exploits sparsity in all imaging dimensions. (3) The CS reconstructed data is processed by utilizing Fleysher combination and applying a Fourier transform along the phase cycle dimension revealed the ^{23}Na MQC spectra, namely single quantum (SQ) and triple quantum (TQ) signal components. Finally, the reconstructed and processed images enable in vivo quantification of Tissue Sodium Concentration (TSC) and/or TQ/SQ ratio.

prior known agar concentrations were performed. Retrospectively undersampled numerical simulations and 3.0 T in vivo data, provided the fully sampled images, were analyzed by means of structural similarity index (SSIM),[46] root mean squared error (RMSE) and signal-to-noise ratio (SNR). For numerical simulations, the metrics were

evaluated over the whole image whereas for the in vivo study, the metrics were computed for the head only.

$$\mathrm{SSIM}(u,\mathrm{ref}) = l(u,\mathrm{ref}) * c(u,\mathrm{ref}) * s(u,\mathrm{ref})$$

$$\mathrm{RMSE}(u,\mathrm{ref}) = \sqrt{\frac{1}{n}\sum_{i=1}^{n}|u_i - \mathrm{ref}_i|^2}$$

$$\mathrm{SNR}(u,\mathrm{ref}) = 20\log_{10}\left(\frac{\overline{u}_{\mathrm{ROI}}}{\sigma_{\mathrm{BG}}}\right), \quad (3)$$

with ref being the fully sampled reference image and SSIM(u,ref) the product of luminescence, $l(u,\mathrm{ref})$, contrast, $c(u,\mathrm{ref})$ and structure, $s(u,\mathrm{ref})$. $\overline{\mathrm{SI}}$ represents mean signal intensity in a specific region. u_{ROI} is the region of interest and u_{BG} is the noise obtained from the background, BG. Normalized intensity complex magnitude images were used to compute the SSIM and the RMSE. For 7.0 T prospectively undersampled data, the relative degree of focus was measured by computing the focus measure as the energy of the Laplacian[47] inside the ROI.

3 | RESULTS

3.1 | Numerical simulations

The realistic numerical simulation of a CRISTINA acquisition from the three-compartment 3D brain enabled to anticipate the SQ and TQ noise levels with and without k-space undersampling (Figure 2). Alternating the sampling masks along the phase-cycle enabled to cover k-space by 82%, 76%, 62%, 50%, 40%, 24% for R = 2–7, respectively. Indeed, 3D and 5D CS improved image reconstruction when compared to zero-filling only. Discrepancies between 3D and 5D CS reconstructions were already observed at an undersampling factor of $R = 3$. Mean TSC values in WM, GM, and CSF were found to be on par: 43 ± 14, 45 ± 21, 132 ± 31 mM for fully sampled, 43 ± 16, 44 ± 20, 118 ± 45 mM for 3D CS and 43 ± 15, 45 ± 22, 131 ± 32 mM for 5D CS reconstructions, respectively. Similarly, mean TQ/SQ ratio values in WM, GM, and CSF were 0.17 ± 0.05, 0.14 ± 0.06, 0.08 ± 0.06 for fully sampled, 0.16 ± 0.05, 0.14 ± 0.06, 0.10 ± 0.07 for 3D CS and $0.17 \pm$

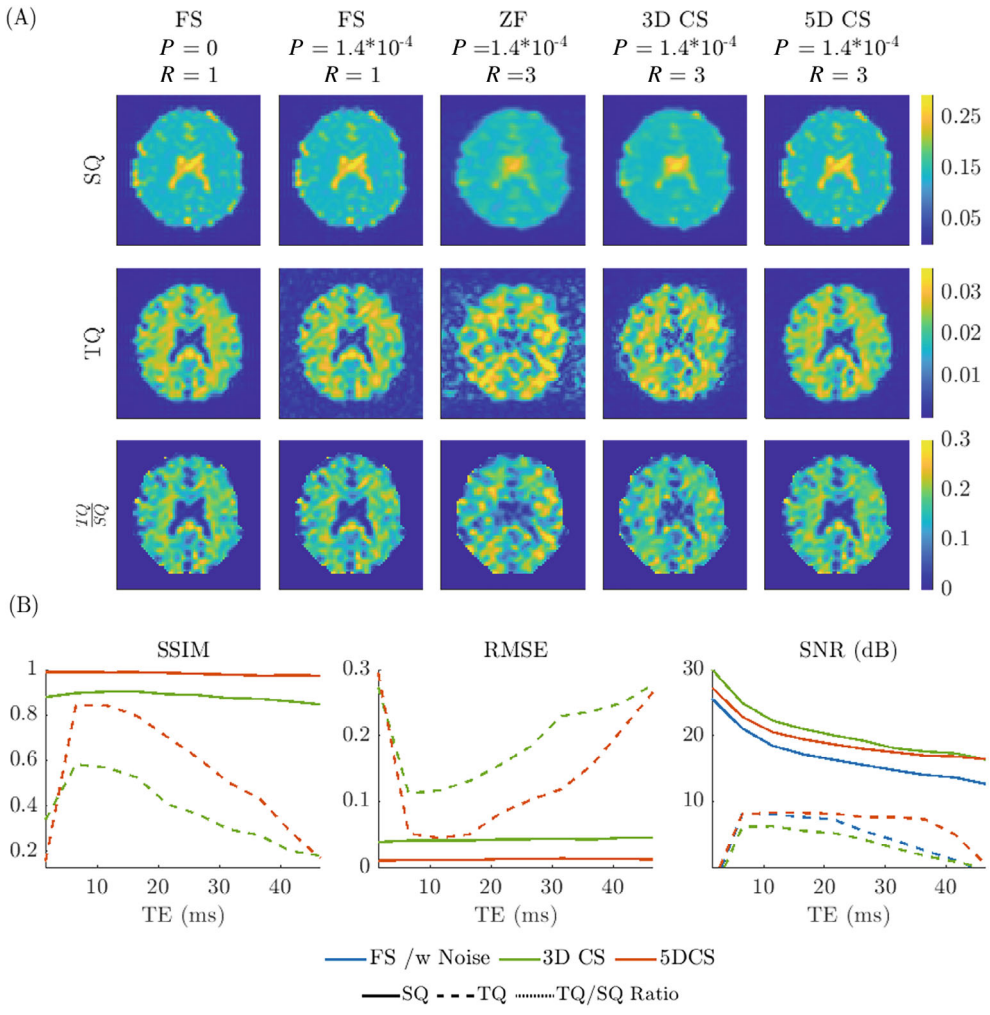

FIGURE 2 (A) Simulated single quantum (SQ), triple quantum (TQ), and TQ/SQ brain data with a nominal resolution of $7 \times 7 \times 10$ mm^3 fully sampled and undersampled with $R = 3$. Noise was added (noise power P=1.4*10^{-4}) and undersampled data were reconstructed with zero-filling, three-dimensional (3D) and five-dimensional (5D) compressed sensing (CS). (B) Quantitative evaluation of reconstruction performance for $R = 3$ via structural similarity index (SSIM), root mean squared error (RMSE), signal-to-noise ratio (SNR) for simulated SQ and TQ brain data depicted in (A).

TABLE 2 Mean and SDs for structural similarity index (SSIM), root mean squared error (RMSE), signal-to-noise ratio (SNR) of reconstructed single quantum (SQ) and triple quantum (TQ).

Model	Signal	SSIM	RMSE	SNR (dB)
(A) In silico				
3D $CS_{R=3}$	SQ	0.88	0.038	30.01
	TQ	0.57	0.117	6.19
	TQ/SQ	0.75	0.052	—
5D $CS_{R=3}$	SQ	0.99	0.010	27.27
	TQ	0.84	0.044	8.28
	TQ/SQ	0.95	0.017	—
3D CS_R	SQ	0.81 ± 0.10	0.057 ± 0.022	—
	TQ	0.56 ± 0.06	0.124 ± 0.024	—
	TQ/SQ	0.74 ± 0.05	0.051 ± 0.008	—
5D CS_R	SQ	0.94 ± 0.07	0.024 ± 0.018	—
	TQ	0.76 ± 0.09	0.081 ± 0.040	—
	TQ/SQ	0.85 ± 0.10	0.029 ± 0.015	—
(B) In vivo				
3D $CS_{R=3}$	SQ	0.93	0.048	29.59
	TQ	0.82	0.094	10.46
	TQ/SQ	0.91	0.024	—
5D $CS_{R=3}$	SQ	0.96	0.023	27.07
	TQ	0.86	0.066	11.54
	TQ/SQ	0.92	0.022	—
3D CS_R	SQ	0.90 ± 0.04	0.065 ± 0.027	—
	TQ	0.84 ± 0.02	0.075 ± 0.014	—
	TQ/SQ	0.89 ± 0.03	0.027 ± 0.005	—
5D CS_R	SQ	0.93 ± 0.04	0.037 ± 0.019	—
	TQ	0.79 ± 0.07	0.097 ± 0.032	—
	TQ/SQ	0.89 ± 0.05	0.027 ± 0.007	—

Notes: $CS_{R=3}$ represents the metrics for $R = 3$ for SQ at TE = 1 or TQ at TE = 3. CS_R represents the metric evaluation averaged over all undersampling factors, $R = 2$–7. Table (A) corresponds to the nummerical simulation (fully sampled: SNR SQ = 25.56 dB, TQ = 7.94 dB) and (B) to the in vivo study performed at 3.0 T (fully sampled: SNR SQ = 22.73 dB, TQ = 8.40 dB).

0.05 and $0.14 \pm 0.06, 0.08 \pm 0.06$ for 5D CS reconstructions, respectively.

All metrics, SSIM, RMSE, and SNR, confirmed 5D CS outperformed 3D CS both along the echo time dimension for $R = 3$ (Figure 2B) or at various undersampling rates (Figure 3B). Mean values and SDs were reported in Table 2A. 5D CS proved to achieve low errors (RMSE) especially at rates $R = 2$ and $R = 3$. Especially for the TQ reconstruction at $R = 3$, 5D CS improved SSIM by 47% and reduced RMSE by 2.5-fold. 5D CS consistently provided improved reconstruction results across all undersampling factors and especially for higher undersampling factors ($R > 3$).

Reconstruction from 5D CS also proved to be more resilient to increased noise level compared to 3D CS (Figure 3A). Mean and SD of SSIM, RMSE, and SNR were given in Table S1. Notably, errors for $R = 3$ TQ images increased almost linearly with noise power for 5D CS. Although TQ signal being of low SNR, 5D CS managed to recover this signal component despite increasing noise levels. Especially remarkable is the consistently improved SSIM and SNR for the TQ signal reconstructed by 5D CS.

3.2 | Phantom study

Image reconstruction from three-fold retrospectively undersampled phantom data acquired at 3.0 T confirmed 5D CS improvement over 3D CS (Figure 4): undersampling artefact were reduced, especially for vials 1-3 and image sharpness was increased. Linear regression (Figure 4C) were confirmed between the SQ signal and

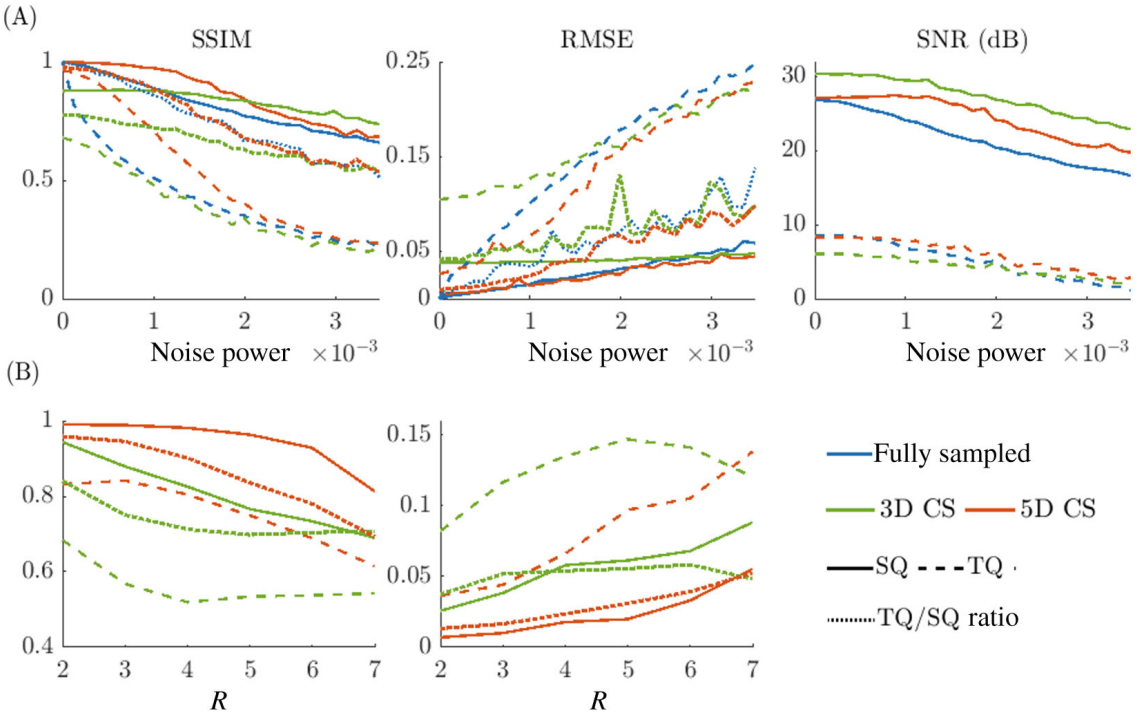

FIGURE 3 Quantitative evaluation of reconstruction performance via structural similarity index (SSIM), root mean squared error (RMSE), signal-to-noise ratio (SNR) for simulated SQ and TQ brain data depicted in Figure 2. (A) Additive noise performance evaluation in regards to SSIM, RMSE and SNR for $R = 3$, with three-dimensional (3D) and five-dimensional (5D) compressed sensing (CS) reconstructed, along increasing noise levels. (B) Reconstruction evaluation for different acceleration factors, R, for 3D and 5D CS models obtained with the same noise power as used in Figure 2.

to the prior known NaCl concentration and between the TQ/SQ ratio and the prior known agar concentration in each vial. The TSC was well preserved in both reconstructions, but the 3D CS TQ/SQ ratio in vials 1 to 3 deviated more from the fully sampled data, indicated by the arrow in the linear regression plot. Fully sampled phantom data exhibited a SNR of 21.93 and 8.26 dB, 3D CS of 27.56 and 6.18 dB, and 5D CS of 28.44 and 13.65 dB for SQ and TQ, respectively. Results of fit parameter maps can be appreciated in supporting information, Figure S5, with a summary of the T_2^* slow and fast components given in Table S3. No significant difference between fully sampled and reconstructed T_2^* values were found for both 3D and 5D CS.

3.3 | 3.0 T in vivo study

It was found that exploiting sparsity along the multi-echo and phase-cycle dimension improved reconstruction results when compared to only exploiting sparsity along either one of the dimensions (Figure S6, Table S1). Results from retrospectively undersampled in vivo ^{23}Na MQC brain data acquired at 3.0 T confirmed the superiority of 5D CS over 3D CS (Figure 5). Images reconstructed by 3D CS exhibited severe blurring, notably the SQ image, and aliasing artifacts, as seen in the TQ image, whereas most features observed in fully sampled images were preserved in images reconstructed by 5D CS. The quantification of TSC and TQ/SQ ratio in the three-compartment WM, GM, and CSF demonstrated minimal discrepancies of region-wise quantification. TSC for fully sampled data was 49 ± 66, 36 ± 41, and 141 ± 123 mM, for 3D CS 54 ± 69, 32 ± 42, and 142 ± 128 mM and for 5D CS 51 ± 67, 34 ± 38, and 141 ± 126 mM, for WM, GM, and CSF, respectively. TQ/SQ ratio was found to be 0.16 ± 0.06, 0.13 ± 0.04, and 0.11 ± 0.05 for fully sampled, 0.15 ± 0.04, 0.14 ± 0.03, and 0.12 ± 0.04 for 3D CS, and 0.16 ± 0.06, 0.13 ± 0.04, and 0.11 ± 0.04 for 5D CS. At an undersampling factor of R = 2, 3D and 5D CS performed similar (Figure 5A). However at $R = 3$, TQ reconstructed with 3D CS exhibited residual undersampling artifacts, which were suppressed in the 5D CS reconstruction. SSIM, RMSE, and SNR evaluated for R=3 along the echo time showed consistently improved performance for the 5D CS model (Figure 5B). With increasing undersampling factor, expected blurring and image degradation was observed. Nevertheless, 5D CS systematically provided higher quality SQ images in contrast to 3D CS, even for high acceleration factors. Quantitative metrics were given in Table 2B.

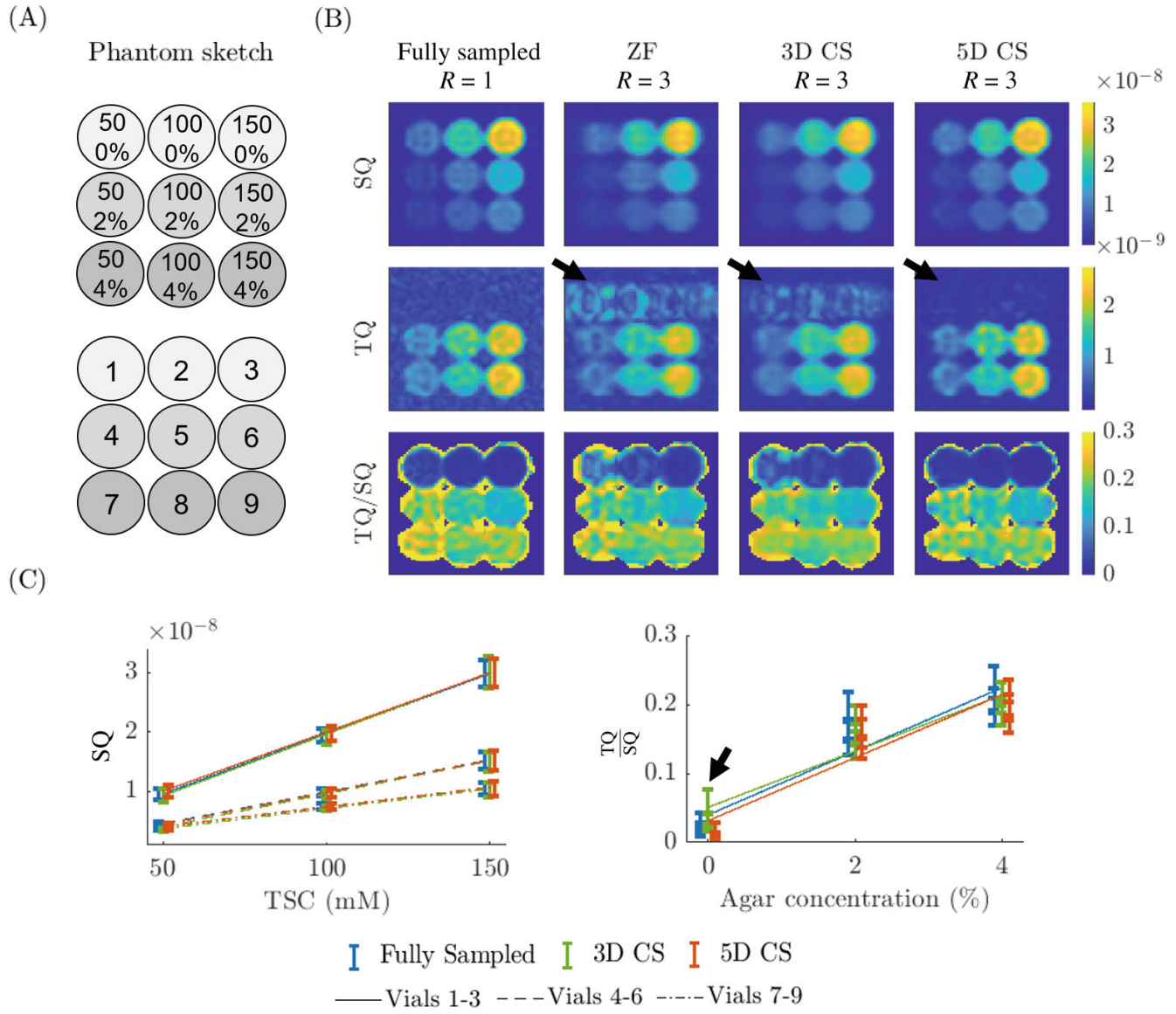

FIGURE 4 Phantom study: (A) Phantom design consisting of 9 different vials (350-mL each) with different NaCl (50, 100, 150-mM) and varying agar concentrations (0%, 2%, and 4%). Phantom vial enumeration for subsequent reconstruction performance evaluation within each vial. (B) single quantum (SQ), triple quantum (TQ), and TQ/SQ ratio comparison of fully sampled, three-dimensional (3D) and five-dimensional (5D) compressed sensing (CS) reconstruction for a retrospective undersampling factor of $R = 3$. SQ and TQ images were fitted with corresponding equations in Equation (2), respectively. Note the residual undersampling artifacts in the 3D CS reconstruction. (C) Shows the linear regression for the mean SQ signal intensity versus prior known TSC in each vial for the fitted data. Data exhibited linear relationships of $R^2 = 0.99^*$ for fully sampled, 3D and 5D CS reconstructed images. Additionally, linear regression was performed on the mean TQ/SQ signal intensity versus known agar concentration in each vial. For the fitted data, linear relationship were found to be $R^2 = 0.84^*$, $R^2 = 0.87^*$, $R^2 = 0.86^*$ for fully sampled, 3D and 5D CS, respectively. With R^2 being the adjusted goodness-of-fit and * representing statistical significance ($p < 0.05$). Computed T_2^* values can be found in Table S3 and Figure S5.

Figure 6 shows three slices of a second volunteer's T_1w ^{1}H and ^{23}Na MQC brain data acquired at 3.0 T and retrospectively undersampled by a factor $R = 3$. Over the multiple slices, SQ images reconstructed with the proposed 5D CS model exhibited less blurring and finer imaging details. Similarly, joint CS reconstruction reduced undersampling-related aliasing artifacts. Additionally, 5D CS provided less erroneous TQ/SQ ratio maps as indicated by the arrow and also improved visual delineation between WM, GM, and CSF. Pushing acceleration further by reducing the number of averages, 5D CS still proved to reconstruct reliable SQ and TQ images within an acquisition time of less than 5 min (Figure S7).

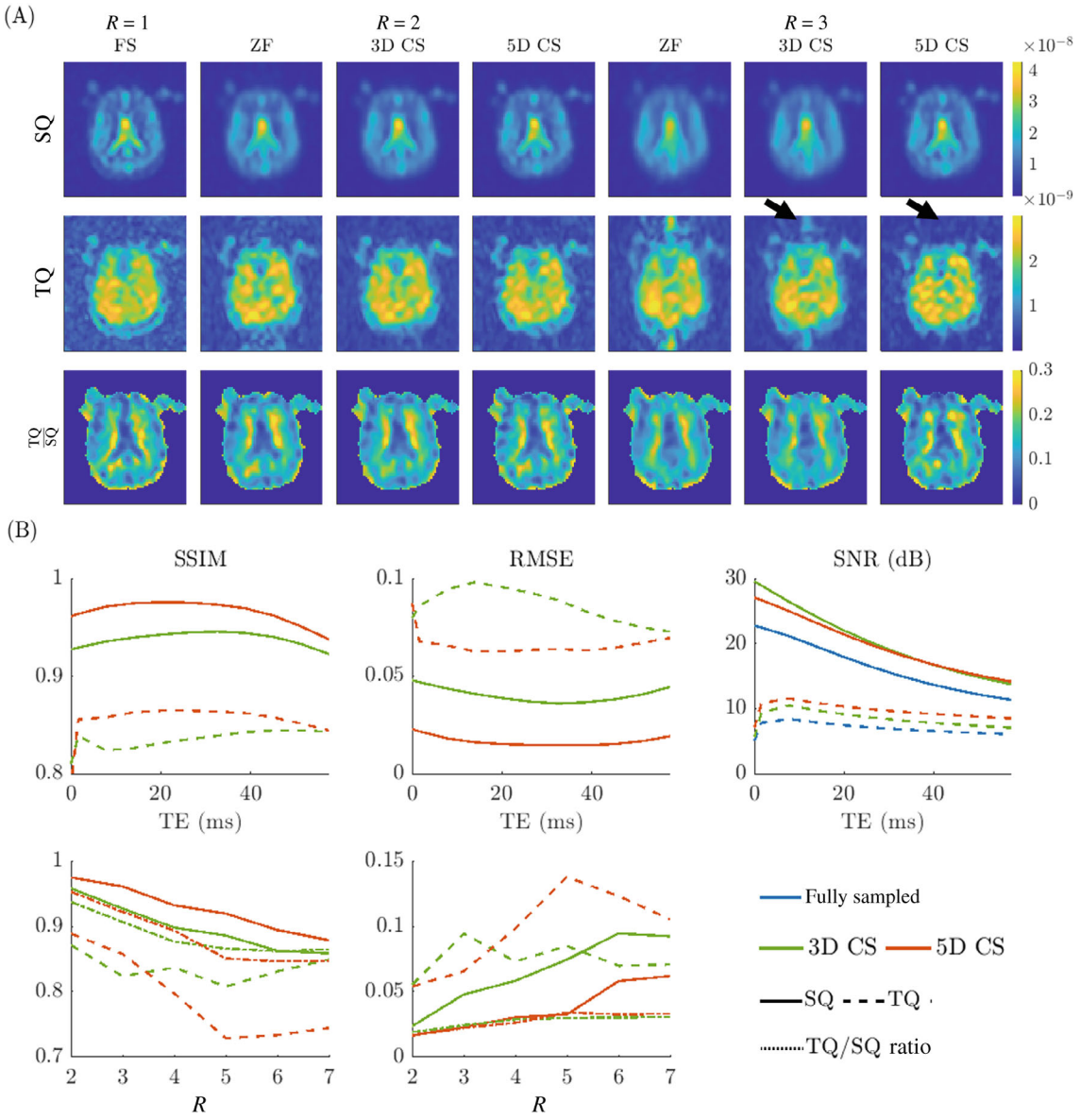

FIGURE 5 (A) Visual representation of reconstruction performance for different undersampling factors, R =2–3, for one volunteer acquired at 3.0 T. (B) In vivo signal-to-noise ratio (SNR), root mean squared error (RMSE), and structural similarity index (SSIM) evaluation over all echoes and for one echo over all undersampling factors for retrospectively undersampled in-vivo brain 3.0 T data are shown.

3.4 | 7.0 T in vivo study

Leveraging a conservative two-fold prospective undersampling, the results of the 7.0 T in vivo study provided unprecedented resolution for MQC ^{23}Na images (Figure 7). Zero-filling yielded blurry SQ and aliased TQ images. 5D CS provided increased SQ image sharpness, which was also confirmed by the focus measure metric: ZF = $2.19 * 10^{-8}$, 3D CS = $2.28 * 10^{-8}$, 5D CS = $2.50 * 10^{-8}$. Additionally, 5D CS reconstructed images provided increased SNR: ZF = 13.10/ 4.56 dB, 3D CS = 13.34/ 6.87 dB, 5D CS = 17.62/ 11.88 dB for SQ and TQ, respectively. The SQ images showed high signal intensity in the CSF compartment whereas the TQ signal mostly originated from the brain parenchyma. Combining these two images, the TQ/SQ ratio for 3D and 5D CS were on par with 5D CS images showing an improved delineation between WM, GM and CSF. It can be appreciated that WM exhibited the highest TQ/SQ ratio 0.21 ± 0.11 and 0.19 ± 0.11, GM intermediate 0.11 ± 0.06 and 0.10 ± 0.06 and CSF the lowest 0.07 ± 0.04 and 0.07 ± 0.05 for 3D and 5D CS, respectively. The improved 3D spatial resolution can also be appreciated in the sagittal and coronal views, where the delineation between the respective compartments is also enhanced by the 5D CS reconstruction.

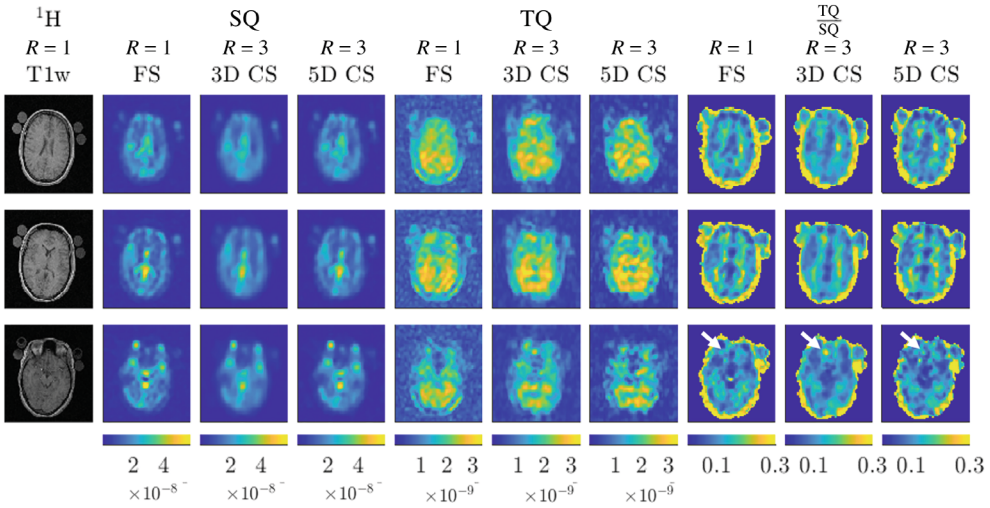

FIGURE 6 Retrospectively three-fold undersampled 3.0 T in-vivo brain data reconstructed with three-dimensional (3D) and five-dimensional (5D) compressed sensing (CS) shown for multiple slices.

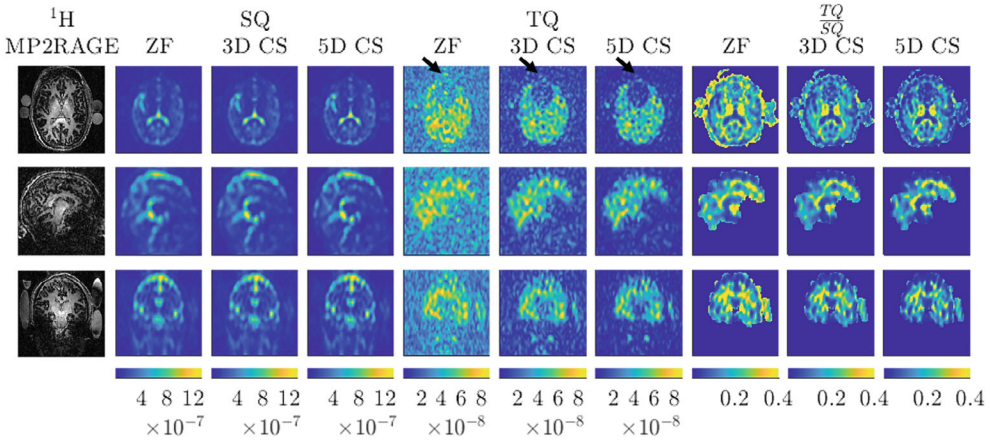

FIGURE 7 Prospectively two-fold undersampled 7.0 T in vivo brain data reconstructed with zero-filling, three-dimensional (3D) and five-dimensional (5D) compressed sensing (CS) shown for transversal, sagittal, and coronal plane with the corresponding anatomical ^{1}H reference images.

4 | DISCUSSION

This study showed that CS could be used for two major limitations of ^{23}Na multi-quantum coherence MRI which are elongated acquisition time and poor spatial resolution. This study evaluated CS for ^{23}Na MQC MRI in four steps. First, a numerical simulation framework allowed to demonstrate the limitations of 3D CS and the necessity to deploy 5D CS for this application. However, numerical simulations, based on a simplistic segmentation of the human brain, lacked realistic data with considerations for imperfect B1^{+}and B0. Second, a calibrated phantom served to confirm experimentally the advantages of 5D CS over 3D CS. Especially, these experiments clearly showed the limitations of 3D CS to provide reliable results in low sodium concentration compartments. Nevertheless, phantom experiments offer beneficial conditions such as large homogeneous regions. Third, a retrospective study was performed on in vivo data acquired at 3.0 T. These data offered the first opportunity to retrospectively test various undersampling rates on in vivo data. The challenge was complete with all the elements to account for: the B1^{+} and B0 relative inhomogeneity, the relatively lower SNR of a 3.0 T sodium head MRI and the elongated scan duration for a fully sampled acquisition. Conventional distance metrics such as SSIM and RMSE did not always reflect visually perceived reconstruction improvement. These reconstruction performance evaluations may not be appropriate since they also take irrelevant structures such as the skull into account, skewing the metric evaluation. Strong from all these incremental validations of our 5D CS framework, a prospectively undersampled in vivo acquisition was implemented. As a fourth step, an unprecedented spatial resolution for ^{23}Na MQC MRI was sought. Alternatively, a shortened acquisition could have been performed although this option was not significantly different from the retrospective study. Eventually, with an undersampling rate of 2, a 2.7-fold reduction of voxel volumes and the boost in SNR thanks to the 7.0 T, whole brain ^{23}Na MQC MRI was acquired with a resolution of $6 \times 6 \times 10$ mm^3. In these images, sharper distinction between gray and white matter MQC properties could be observed.

4.1 | 7.0 T in vivo study

Transitioning from 3.0 to 7.0 T boosted the SNR, enabling potentially higher acceleration. However, higher field strengths come with stricter SAR limitations, adversely prolonging acquisition due to increased TR and diminishing the benefits of ultra-high field ^{23}Na MQC MRI. Moreover, the TQ signal is highly dependent on $B1^+$ as it scales with $\sin^5(\alpha)$, further penalizing 7.0 T acquisitions. Future work could utilize flip angle mapping for $B1^+$ postprocessing correction.[22] This study only considered dual-tuned birdcage coils with single transmit and receive channels, both at 3.0 and 7.0 T. Utilizing multireceive channels could further push acceleration possibilities thanks to SNR improvements and by simultaneously leveraging parallel acquisition techniques.[48]

4.2 | Potential extensions to proposed image reconstruction

One further improvement could be to change the sampling pattern more frequently, for example, for each repetition and/or along echo time, thus enabling to reduce the amount of fully sampled center region and hence, to increase incoherence. CRISTINA phase-cycle leverages a total of 2×6 steps for the Fleysher combination[36] to compensate for B0 inhomogeneity-induced signal loss occurring during the evolution time. In the current implementation, to accommodate the Fleysher combination, both data sets χ_0 and χ_{90} are identically undersampled. To further push acceleration, one could consider undersampling each data set differently and combining them to extend the phase cycle dimension for CS reconstruction, albeit with a different transform than the Fourier transform employed in our algorithm.

Another extension from the proposed CS model could be to exploit joint constraints across the multidimensional space instead of individual constraints. The chosen separated framework permitted independent scaling of each regularization term, allowing tuning them for optimal reconstruction results since sparsity might differ among the 5 dimensions. Another joint approach could be tensor sparsity, to leverage multidimensional sparsity simultaneously as proposed by Yu et al.[49] or Roohi et al.[50] Additionally, improved reconstruction might be achievable by exploiting k-space similarity such as in LORAKS[51] or SAKE[52] and thus not limiting the reconstruction to sparsity assumptions only. It is also noteworthy that CS reconstruction performances are highly dependent on the initial SNR of the signal. Hence, reconstruction performances and achievable acceleration factors are highly limited by ^{23}Na MQC MRI's intrinsically poor SNR, yielding noisy images even though fully sampled k-space was acquired. Following, spatial TV sparsity could be improved by leveraging anatomical prior constraints as proposed by Gnahm et al.,[29] Lachner et al.,[27] and Zhao et al.[53]

Another limitation of ^{23}Na MQC MRI is that its TSC differs from the TSC measured by conventional ^{23}Na MRI. Indeed, CRISTINA's apparent TSC is affected by T_2^* due to the long evolution time. A more accurate TSC estimation could be obtained by using an additional readout during the evolution time by leveraging a UTE readout as included in the SISTINA[19] method. Following the work of Aldung et al.[54], the CSF was used as reference in-vivo to quantify TSC since it is less affected by $B1^+$ inhomogeneity and noise due to short T_2 components compared to external vials placed at the edges of the coil with agar content reducing their T_2 values.

4.3 | Alternatives for improved image reconstruction

First, further reconstruction improvements could be expected by leveraging convolutional neural networks as proposed by Adlung et al.[31] In particular, deep learning techniques could be used to find optimal sparse representations of the signal.[55] Joint frameworks combining Deep Learning and CS have also shown promising results in regards to reduced reconstruction time[56] or overall enhanced reconstruction quality by exploiting relevant features in the images.[57] Nevertheless, the performance highly depends on the amount of training data, which remains limited for ^{23}Na MQC MRI.

Second, reconstruction parameters were determined empirically based on SSIM and RMSE assessment. Due to the intrinsic low SNR of the signal, optimization of reconstruction parameters was challenging. Further research could utilize Automated Parameter Selection for Accelerated MRI Reconstruction as proposed by Ilicak et al.[58] Furthermore, estimating the noise floor and computing the sparsity threshold with respect to this parameter could help to find optimal sparsity thresholds for each dimension.

Third, the here presented workflow was separated into image reconstruction (CS) and image postprocessing, which consisted of Fleysher combination and model-based reconstruction of fitting the signal equations (Equation 2). Future work could evaluate the benefits of combining these steps by leveraging CS coupled with a model-based reconstruction[59] that incorporates SQ and TQ signal fitting into CS. The here presented 5D CS model exploits shared information of the superimposed ^{23}Na MQC signal and the spectrum by computing the one-dimensional Fourier transform along the phase-cycling dimension. Hence, the proposed 5D CS algorithm could easily be extended, with additions for T_2^* signal decay, to a model-based image

reconstruction that takes relevant physical parameters into account and leverages the theoretical SQ and TQ signal models. However, these model-based approaches add another level of complexity and risk overfitting,[59] which was deemed beyond the scope of this study.

Finally, CRISTINA sequence is based on Cartesian readouts, which are SNR efficient since they sample k-space more evenly. Alternatively, non-Cartesian readouts might be better suited to full fill the prerequisite of incoherent undersampling noise required for CS. Nevertheless, Cartesian sampling eases reconstruction procedure, notably memory when handling large datasets, and is more robust to hardware imperfections, potentially fostering reproducibility across different platforms. Furthermore, alternating the sampling patterns along the phase cycle dimension promoted incoherent undersampling artifacts thus, better satisfying CS reconstruction theory. Further acceleration, however, could be achieved by leveraging Twisted Projection Imaging[60] or density-adapted[61] radial k-space sampling, due to the fact that these methods provide increased initial SNR and additionally, enhance sampling randomness. However, the 3D variable density Cartesian sampling technique has already demonstrated potential in multiple CS applications. Furthermore, the proposed multi-dimensional CS model's strength lies in the regularization of the phase-cycle dimension, which would be similar between Cartesian and non-Cartesian sampling trajectories. Finally, paired with a strong asymmetric first echo, ^{23}Na MQC signal Cartesian sampling could be performed with a short first echo time, benefiting SQ signal. Later echoes were fully sampled to balance the lower SNR, especially for sampling the TQ signal.

5 | CONCLUSION

A dedicated CS reconstruction exploiting 3D spatial sparsity and sparsity along echo and phase-cycle dimension was demonstrated to allow undersampling of Cartesian ^{23}Na MQC MRI. Numerical simulations, retrospective and prospective phantom and in vivo analysis of reconstruction performance revealed suitable acceleration factors of up to 3-fold to either accelerate acquisition to obtain ^{23}Na MQC MR images within less than 5 min at 3.0 T or to increase spatial resolution up to $6 \times 6 \times 10$ mm^3 at 7.0 T without extending imaging time or compromising image quality.

ACKNOWLEDGMENTS

The research was supported by the ISMRM Research Exchange grant 2022 and the PROCOPE Mobility grant 2022. This study received funding from the French government under the "Programme d'Investissement d'Avenir", Excellence Initiative of Aix-Marseille University-A*MIDEX (AMX-19IET-004), 7 TEAMS Chair. Open Access funding enabled and organized by Projekt DEAL.

CONFLICT OF INTEREST STATEMENT

The authors declare no potential conflict of interests.

DATA AVAILABILITY STATEMENT

A processing code for the CS and image processing for CRISTINA ^{23}Na MQC MRI will be made available at https://github.com/c-licht/23Na-MQC-MRI. The experimental data are not publicly available due to ethics restrictions.

ORCID

Christian Licht https://orcid.org/0000-0001-7454-3735
Simon Reichert https://orcid.org/0000-0002-6013-8242
Stanislas Rapacchi https://orcid.org/0000-0002-8925-495X

REFERENCES

1. Ouwerkerk R, Bleich K, Gillen J, Pomper M, Bottomley P. Tissue sodium concentration in human brain tumors as measured with 23Na MR imaging. *Radiology*. 2003;227:529-537.
2. Lu A, Atkinson IC, Thulborn KR. Sodium magnetic resonance imaging and its bioscale of tissue sodium concentration. In: Harris RK, Wasylishen RE, eds. *Encyclopedia of magnetic resonance*. Wiley; 2010:1-15.
3. Thulborn K. Quantitative sodium MR imaging: a review of its evolving role in medicine. *Neuroimage*. 2016;168:250-268.
4. Madelin G, Lee J, Regatte R, Jerschow A. Sodium MRI: methods and applications. *Prog Nucl Magn Reson Spectrosc*. 2014;79:14-47. https://www.sciencedirect.com/science/article/pii/S0079656514000211
5. Thulborn K, Davis D, Adams H, Gindin T, Zhou J. Quantitative tissue sodium concentration mapping of the growth of focal cerebral tumors with sodium magnetic resonance imaging. *Magn Reson Med*. 1999;41:351-359.
6. Hilal S, Maudsley A, Ra J, et al. In vivo NMR imaging of sodium-23 in the human head. *J Comput Assist Tomogr*. 1985;9:1-7.
7. Zaric O, Beiglböck H, Janacova V, et al. Repeatability assessment of sodium (23Na) MRI at 7.0 T in healthy human calf muscle and preliminary results on tissue sodium concentrations in subjects with Addison's disease. *BMC Musculoskelet Disord*. 2022;23:925. doi:10.1186/s12891-022-05879-5
8. Madelin G, Regatte R. Biomedical applications of sodium MRI in vivo. *J Magn Reson Imag*. 2013;38:511-529. https://pubmed.ncbi.nlm.nih.gov/23722972
9. Poku L, Phil M, Cheng Y, Wang K, Sun X. 23Na-MRI as a noninvasive biomarker for cancer diagnosis and prognosis. *J Magn Reson Imaging*. 2021;53:995-1014. https://onlinelibrary.wiley.com/doi/abs/10.1002/jmri.27147
10. Nunes Neto L, Madelin G, Sood T, et al. Quantitative sodium imaging and gliomas: a feasibility study. *Neuroradiology*. 2018;60:795-802. https://pubmed.ncbi.nlm.nih.gov/29862413

11. Regnery S, Behl N, Platt T, et al. Ultra-high-field sodium MRI as biomarker for tumor extent, grade and IDH mutation status in glioma patients. *NeuroImage Clin*. 2020;28:102427. https://www.sciencedirect.com/science/article/pii/S2213158220302643
12. Mohamed S, Herrmann K, Adlung A, et al. Evaluation of sodium ((23)Na) MR-imaging as a biomarker and predictor for neurodegenerative changes in patients with Alzheimer's disease. *In Vivo (Athens, Greece)*. 2021;35:429-435. https://pubmed.ncbi.nlm.nih.gov/33402493
13. Huhn K, Engelhorn T, Linker R, Nagel A. Potential of sodium MRI as a biomarker for neurodegeneration and neuroinflammation in multiple sclerosis. *Front Neurol*. 2019;10:84. https://pubmed.ncbi.nlm.nih.gov/30804885
14. Stobbe R, Boyd A, Smyth P, Emery D, Valdés Cabrera D, Beaulieu C. Sodium intensity changes differ between relaxation- and density-weighted MRI in multiple sclerosis. *Front Neurol*. 2021;12:693447. doi:10.3389/fneur.2021.693447
15. Rooney W, Springer C. A comprehensive approach to the analysis and interpretation of the resonances of spins 3/2 from living systems. *NMR Biomed*. 1991;4:209-226.
16. LaVerde G, Nemoto E, Jungreis C, Tanase C, Boada F. Serial triple quantum sodium MRI during non-human primate focal brain ischemia. *Magn Reson Med*. 2007;57:201-205. https://onlinelibrary.wiley.com/doi/abs/10.1002/mrm.21087
17. Schepkin V, Choy I, Budinger T, et al. Sodium TQF NMR and intracellular sodium in isolated crystalloid perfused rat heart. *Magn Reson Med*. 1998;39:557-563. https://onlinelibrary.wiley.com/doi/abs/10.1002/mrm.1910390408
18. Hoesl M, Schad L, Rapacchi S. Efficient 23Na triple-quantum signal imaging on clinical scanners: Cartesian imaging of single and triple-quantum 23Na (CRISTINA). *Magn Reson Med*. 2020;84:2412-2428. https://onlinelibrary.wiley.com/doi/abs/10.1002/mrm.28284
19. Fiege D, Romanzetti S, Mirkes C, Brenner D, Shah N. Simultaneous single-quantum and triple-quantum-filtered MRI of 23Na (SISTINA). *Magn Reson Med*. 2013;69:1691-1696. https://onlinelibrary.wiley.com/doi/abs/10.1002/mrm.24417
20. Tsang A, Stobbe R, Beaulieu C. Triple-quantum-filtered sodium imaging of the human brain at 4.7 T. *Magn Reson Med*. 2012;67:1633-1643. https://onlinelibrary.wiley.com/doi/abs/10.1002/mrm.23147
21. Hancu I, Boada F, Shen G. Three-dimensional triple-quantum–filtered 23Na imaging of in vivo human brain. *Magn Reson Med*. 1999;42:1146-1154. https://onlinelibrary.wiley.com/doi/abs/10.1002/%28SICI%291522-2594%28199912%2942%3A6%3C1146%3A%3AAID-MRM20%3E3.0.CO%3B2-S
22. Borthakur A, Hancu I, Boada F, Shen G, Shapiro E, Reddy R. In vivo triple quantum filtered twisted projection sodium MRI of human articular cartilage. *J Magn Reson*. 1999;141:286-290. https://www.sciencedirect.com/science/article/pii/S1090780799919237
23. Ooms K, Cannella M, Vega A, Marcolongo M, Polenova T. 23Na TQF NMR imaging for the study of spinal disc tissue. *J Magn Reson*. 2008;195:112-115. https://www.sciencedirect.com/science/article/pii/S1090780708002450
24. Boada F, Davis D, Walter K, et al. Triple quantum filtered sodium MRI of primary brain tumors. *2004 2nd IEEE International Symposium on Biomedical Imaging: Nano to Macro (IEEE Cat No. 04EX821)*. Vol 2. IEEE; 2004:1215-1218.
25. Lustig M, Donoho D, Pauly J. Sparse MRI: the application of compressed sensing for rapid MR imaging. *Magn Reson Med*. 2007;58:1182-1195. https://onlinelibrary.wiley.com/doi/abs/10.1002/mrm.21391
26. Madelin G, Chang G, Otazo R, Jerschow A, Regatte R. Compressed sensing sodium MRI of cartilage at 7T: preliminary study. *J Magn Reson*. 2012;214:360-365. https://pubmed.ncbi.nlm.nih.gov/22204825
27. Lachner S, Zaric O, Utzschneider M, et al. Compressed sensing reconstruction of 7 tesla 23Na multi-channel breast data using 1H MRI constraint. *Magn Reson Imaging*. 2019;60:145-156. https://www.sciencedirect.com/science/article/pii/S0730725X18306167
28. Behl N, Gnahm C, Bachert P, Ladd M, Nagel A. Three-dimensional dictionary-learning reconstruction of 23Na MRI data. *Magn Reson Med*. 2016;75:1605-1616. https://onlinelibrary.wiley.com/doi/abs/10.1002/mrm.25759
29. Gnahm C, Nagel A. Anatomically weighted second-order total variation reconstruction of 23Na MRI using prior information from 1H MRI. *Neuroimage*. 2015;105:452-461. https://www.sciencedirect.com/science/article/pii/S1053811914009082
30. Weingärtner S, Wetterling F, Konstandin S, Fatar M, Neumaier-Probst E, Schad L. Scan time reduction in 23Na-magnetic resonance imaging using the chemical shift imaging sequence: evaluation of an iterative reconstruction method. *Z Med Phys*. 2015;25:275-286. https://www.sciencedirect.com/science/article/pii/S0939388914001020
31. Adlung A, Paschke N, Golla A, et al. (23) Na MRI in ischemic stroke: acquisition time reduction using postprocessing with convolutional neural networks. *NMR Biomed*. 2021;34:e4474.
32. Candes E, Romberg J, Tao T. Robust uncertainty principles: exact signal reconstruction from highly incomplete frequency information. *IEEE Trans Inform Theory*. 2006;52:489-509.
33. Montesinos P, Abascal J, Cussó L, Vaquero J, Desco M. Application of the compressed sensing technique to self-gated cardiac cine sequences in small animals. *Magn Reson Med*. 2014;72:369-380. https://onlinelibrary.wiley.com/doi/abs/10.1002/mrm.24936
34. Rudin L, Osher S, Fatemi E. Nonlinear total variation based noise removal algorithms. *Phys D Nonlinear Phenomena*. 1992;60:259-268. https://www.sciencedirect.com/science/article/pii/016727899290242F
35. Lustig M, Santos J, Donoho D. Kt SPARSE: high frame rate dynamic MRI exploiting spatio-temporal sparsity. *Proc 13th ISMRM*. 2006;50:2003.
36. Fleysher L, Oesingmann N, Inglese M. B0 inhomogeneity-insensitive triple-quantum-filtered sodium imaging using a 12-step phase-cycling scheme. *NMR Biomed*. 2010;23:1191-1198. https://analyticalsciencejournals.onlinelibrary.wiley.com/doi/abs/10.1002/nbm.1548
37. Collins D, Zijdenbos A, Kollokian V, et al. Design and construction of a realistic digital brain phantom. *IEEE Trans Med Imaging*. 1998;17:463-468.
38. Blunck Y, Josan S, Taqdees S, et al. 3D-multi-echo radial imaging of 23Na (3D-MERINA) for time-efficient multi-parameter tissue compartment mapping. *Magn Reson Med*. 2018;79:1950-1961. https://onlinelibrary.wiley.com/doi/abs/10.1002/mrm.26848
39. Hancu I, Maarel J, Boada F. A model for the dynamics of spins 3/2 in biological media: signal loss during radiofrequency

excitation in triple-quantum-filtered sodium MRI. *J Magn Reson*. 2000;147:179-191.
40. Maarel J. Thermal relaxation and coherence dynamics of spin 3/2. I static and fluctuating quadrupolar interactions in the multipole basis. *Concepts Magn Reson Pt A*. 2003;19A:97-116. https://onlinelibrary.wiley.com/doi/abs/10.1002/cmr.a.10087
41. Hoesl MAU, Schad LR, Rapacchi S. Volumetric 23Na single and triple-quantum imaging at 7T: 3D-CRISTINA. *Z Med Phys*. 2022;32(2):199-208.
42. Schepkin V, Neubauer A, Nagel A, Budinger T. Comparison of potassium and sodium binding in vivo and in agarose samples using TQTPPI pulse sequence. *J Magn Reson*. 2017;277:162-168. https://www.sciencedirect.com/science/article/pii/S1090780717300642
43. Marques J, Kober T, Krueger G, Van der Zwaag W, Van de Moortele P, Gruetter R. MP2RAGE, a self bias-field corrected sequence for improved segmentation and T1-mapping at high field. *Neuroimage*. 2010;49:1271-1281. https://www.sciencedirect.com/science/article/pii/S1053811909010738
44. Küstner T, Schwartz M, Würslin C, et al. Compressed sensing LAB: an MR acquisition and reconstruction system. In Proceedings of the ISMRM Workshop on Data Sampling and Reconstruction, Sedona, AZ, USA; 2016.
45. Goldstein T, Osher S. The Split Bregman method for L1-regularized problems. *SIAM J Imag Sci*. 2009;2:323-343. doi:10.1137/080725891
46. Wang Z, Bovik A, Sheikh H, Simoncelli E. Image quality assessment: from error visibility to structural similarity. *IEEE Trans Image Process*. 2004;13:600-612.
47. Subbarao M, Tyan J. Selecting the optimal focus measure for autofocusing and depth-from-focus. *IEEE Trans Pattern Anal Mach Intell*. 1998;20:864-870.
48. Lachner S, Utzschneider M, Zaric O, et al. Compressed sensing and the use of phased array coils in 23Na MRI: a comparison of a SENSE-based and an individually combined multi-channel reconstruction. *Z Med Phys*. 2021;31:48-57. https://www.sciencedirect.com/science/article/pii/S0939388920301057
49. Yu Y. Multidimensional compressed sensing MRI using tensor decomposition-based Sparsifying transform. *PloS One*. 2014;9:1-13. doi:10.1371/journal.pone.0098441
50. Roohi SF, Zonoobi D, Kassim AA, Jaremko JL. Dynamic MRI reconstruction using low rank plus sparse tensor decomposition. 2016 IEEE International Conference on Image Processing (ICIP), Phoenix, AZ, USA; 2016:1769-1773. doi:10.1109/ICIP.2016.7532662
51. Haldar J. Low-rank modeling of local k-space neighborhoods (LORAKS) for constrained MRI. *IEEE Trans Med Imaging*. 2014;33:668-681.
52. Shin P, Larson P, Ohliger M, et al. Calibrationless parallel imaging reconstruction based on structured low-rank matrix completion. *Magn Reson Med*. 2013;72:959-970.
53. Zhao Y, Guo R, Li Y, Thulborn K, Liang Z. High-resolution sodium imaging using anatomical and sparsity constraints for denoising and recovery of novel features. *Magn Reson Med*. 2021;86:625-636. https://onlinelibrary.wiley.com/doi/abs/10.1002/mrm.28767
54. Adlung A, Licht C, Reichert S, et al. Quantification of tissue sodium concentration in the ischemic stroke: a comparison between external and internal references for 23Na MRI. *J Neurosci Methods*. 2022;382:109721. https://www.sciencedirect.com/science/article/pii/S0165027022002473
55. Gregor K, LeCun Y. Learning fast approximations of sparse coding. In Proceedings of the 27th International Conference on International Conference on Machine Learning (ICML'10). Omnipress, Madison, WI, USA; 2010:399-406.
56. Kulkarni K, Lohit S, Turaga P, Kerviche R, Ashok A. Reconnet: non-iterative reconstruction of images from compressively sensed measurements. In 2016 IEEE Conference on Computer Vision and Pattern Recognition (CVPR), Las Vegas, NV, USA; 2016:449-458.doi:10.1109/CVPR.2016.55
57. Machidon A, Pejović V. Deep learning for compressive sensing: a ubiquitous systems perspective. *Artif Intell Rev*. 2023;56:3619-3658.
58. Ilicak E, Saritas EEU, Cukur T. Automated parameter selection for accelerated MRI reconstruction via low-rank modeling of local k-space neighborhoods. *Z Med Phys*. 2023;33(2):203-219.
59. Fessler J. Model-based image reconstruction for MRI. *IEEE Signal Process Mag*. 2010;27:81-89.
60. Boada F, Gillen J, Shen G, Chang S, Thulborn K. Fast three dimensional sodium imaging. *Magn Reson Med*. 1997;37:706-715. https://onlinelibrary.wiley.com/doi/abs/10.1002/mrm.1910370512
61. Nagel A, Laun F, Weber M, Matthies C, Semmler W, Schad L. Sodium MRI using a density-adapted 3D radial acquisition technique. *Magn Reson Med*. 2009;62:1565-1573.

SUPPORTING INFORMATION

Additional supporting information may be found in the online version of the article at the publisher's website.

Figure S1. Reconstruction evaluation of Wavelet and TV sparsifying transform. It was found that WT and TV performed similar and therefore, we chose to utilize TV as the spatial sparsifying transform.

Figure S2. Demonstration of sparsity along the phase-cycling (A) and along the multi-echo, TE (B). (A) Performing the Fourier transform along the phase-cycle dimension reveals the ^{23}Na MQC spectrum. The TQ image is depicted in image ϕ_1 and the SQ images are shown in images ϕ_3 and ϕ_5. It is demonstrated that the images at index 2 and 6 are pure noise, which shows that the image is sparser in the transformed domain. Additionally, the Fourier transform enables to regularize on the ^{23}Na MQC spectrum directly, which further improves reconstruction performance by enabling to tune the reconstruction towards either SQ or TQ signal component. (B) Performing a Fourier transform along the multi-echo dimension reveals the dominant Fourier coefficients, depicted at the center (TE_5). Smaller Fourier coefficients represent noise and are shown in TE_1, TE_9 and TE_{10}. Conclusively, applying the Fourier transform along the echo time and the phase-cycle dimension results in sparser images, which reduce the complexity of the optimization problem. This sparsity is exploited within the additional

regularization terms of the 5D CS model to find a better solution.

Figure S3. Color plots of all metrics for different sparsity thresholds for the multi-echo dimension (β_{TE}) and the phase-cycle dimension (β_ϕ) evaluated on 3-fold undersampled numerical simulations. The square in red shows the regularization parameter combination that provided the best reconstruction result. It is demonstrated that the phase-cycling dimension can be made sparser than the multi-echo dimension. Additionally, the graphs demonstrate that a variety of different values lead to high reconstruction quality. It is also shown that not regularizing the phase-cycle dimension (β_ϕ=0) leads to decreased reconstruction performance, whereas small thresholds are beneficial for TE regularization. Conclusively, a trade-off between optimal SSIM, RMSE and SNR was found by using β_{TE}=0.4 and β_ϕ=2.0.

Figure S4. Color plots of all metrics for different regularization term weightings for the multi-echo dimension (λ_{TE}) and the phase-cycle dimension (λ_ϕ) evaluated on 3-fold undersampled numerical simulations. The square in red shows the regularization parameter combination that provided the best reconstruction result. The graphs revealed that a variety of different values lead to high reconstruction quality. It was also shown that decreasing the weight of the TE regularization lead to decreased reconstruction performance, whereas smaller weights were beneficial for phase-cycle regularization. Interestingly, overweighting the regularization factors (λ_ϕ, $\lambda_{TE} > 1$) results in decreased reconstruction performance. Conclusively, a trade-off between optimal SSIM, RMSE and SNR was found by using λ_{TE}=1.6 and λ_ϕ=0.7.

Figure S5. Resulting fit parameter maps for a center slice of fully sampled, 3D and 5D CS reconstructions obtained with an undersampling factor of R=3 (Figure 4). Maps are shown with a body mask. It can be appreciated that vials containing 2 or 4% agar gel exhibit shorter T_2^* components as well as larger TQ signal amplitudes. A_{SQ_2} exhibited strong artefacts for the first row of vials, which do not contain agar. Hence, no T2f component is expected yielding a noisy A_{SQ_2} parameter fit map. This artefact is even stronger for the 3D CS reconstruction due to the residual aliasing artefact. Additionally, the 3D CS parameters maps revealed extended blurring when compared to fully sampled and 5D CS.

Figure S6. Reconstruction performance with different regularization terms added. It is noteworthy that improved reconstruction was already observed by adding one of each regularization term (TE or ϕ). However, best performance was obtained when both regularization terms, e.g. 5D CS, were utilized. Quantitative metrics are given in Table S1.

Figure S7. Reconstruction performance of 3D and 5D CS for R=3 and reduced averages. Reducing the number of averages enabled further acceleration, but degraded image quality. However, 5D CS yielded reliable SQ and TQ/SQ ratio image reconstruction up to an acquisition time of less than 5 minutes.

Table S1. Quantitative reconstruction evaluation for 3D, 4D and 5D CS models that utilize different regularization terms. 5D CS demonstrated to provide superior reconstruction quality. Images are shown in Figure S6.

Table S2. Mean and standard deviations for SSIM, RMSE and SNR of simulated fully sampled and 3-fold undersampled SQ and TQ data for different noise levels. Metrics were evaluated against noise-free fully sampled data.

Table S3. Mean and standard deviations for T_2^* fast and slow components (ms) of the shown slice in Figure S5 reconstructed with 3D and 5D CS at an undersampling factor of R=3.

How to cite this article: Licht C, Reichert S, Guye M, Schad LR, Rapacchi S. Multidimensional compressed sensing to advance ^{23}Na multi-quantum coherences MRI. *Magn Reson Med*. 2023;1-16. doi: 10.1002/mrm.29902